PROGRESSIVE DAMAGE ANALYSES OF SKIN/STRINGER DEBONDING

C. G. Dávila, P. P. Camanho, and M. F. de Moura

Abstract

The debonding of skin/stringer constructions is analyzed using a step-by-step simulation of material degradation based on strain softening decohesion elements and a ply degradation procedure. Decohesion elements with mixed-mode capability are placed at the interface between the skin and the flange to simulate the initiation and propagation of the delamination. In addition, the initiation and accumulation of fiber failure and matrix damage is modeled using Hashin-type failure criteria and their corresponding material degradation schedules. The debonding predictions using simplified three-dimensional models correlate well with test results.

INTRODUCTION

The fracture process of high performance composite laminates is quite complex, involving both intralaminar damage mechanisms (e.g. matrix cracking, fiber fracture) and interlaminar damage (delamination). The basic failure mechanisms that can induce failure in a laminated composite are: matrix tensile/compressive cracking, fiber-matrix shearing, fiber tensile failure, fiber microbuckling, and delamination. To simulate damage growth accurately, a failure analysis must be able to predict all failure modes and apply a corresponding reduction in material stiffness.

The objective of the proposed paper is to demonstrate a methodology that can calculate the strength of composite structures by predicting the growth of all major damage modes, including delamination and ply damage. The effectiveness of the methodology for modeling the debonding of skin/stringer is assessed. The failure of these specimens is clearly dominated by delamination. However, other damage mechanisms such as transverse matrix cracking are also present and the simulation of their interaction with the initiation and growth of delamination needs to be included in the analyses. Delamination is simulated with decohesion elements and ply damage is simulated by degrading the elastic properties after a failure criterion has been exceeded.

Carlos G. Davilla, NASA Langley Research Center, MS 240, Hampton, VA.
Pedro P. Camanho and Marcelo F. de Moura, Faculdade de Engenharia – DEMEGI (SMAP), Rua Dr. Roberto Frias, s/n, 4200-465 Porto, Portugal.

DECOHESION ELEMENTS

Decohesion elements are well suited to progressive failure analyses where both ply damage and delaminations are present. The approach consists of placing interfacial decohesion elements between composite layers. A decohesion failure criterion that combines aspects of strength-based analysis and fracture mechanics is used to simulate debonding by softening the element. The constitutive equations for the interface are phenomenological mechanical relations between the tractions and interfacial separations. With increasing interfacial separation, the tractions across the interface reach a maximum, decrease, and vanish when complete decohesion occurs. The work of normal and tangential separation can be related to the critical values of energy release rates.

The decohesion elements are used to model the interface between sublaminates or between two bonded components. An 8-node decohesion element shown in Fig. 1 was developed and implemented in the ABAQUS finite element code. The element is a zero-thickness volumetric element in which the interpolating shape functions for the top and bottom faces are compatible with the kinematics of the elements that are being connected to it. Details of the development of this element are presented in Refs. 1 and 2.

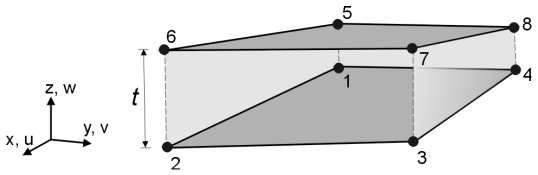

Figure 1. Eight-node decohesion element; t≈0.

Constitutive Equations of Decohesion

A constitutive equation is used to relate the traction σ to the relative displacement δ at the interface. Some strain softening models that have been proposed are shown in Fig. 2 and include: linear elastic-perfectly plastic; linear elastic-linear softening; linear elastic-progressive softening; linear elastic-regressive softening; and Needleman [3]. One characteristic of all softening models is that the cohesive zone can still transfer load after the onset of damage (δ^o in Fig. 2). For pure Mode I, II or III loading, after the interfacial normal or shear tractions attain their respective interlaminar tensile or shear strengths, the stiffnesses are gradually reduced to zero. The area under the traction-relative displacement curves is the corresponding (Mode I, II or III) fracture energy. Using the definition of the *J* integral proposed by Rice [4], and evaluating the integral *J* on the contour defined by the cohesive zone, the relationship

$$\int_0^{\delta^F} \sigma(\delta) d\delta = G_C \tag{1}$$

is obtained, where G_c is the critical energy release rate for a particular mode and δ^F is the corresponding relative displacement at failure (δ_{pp}, δ_{pro}, δ_{lin} δ_{Ne}, or δ_{re} in Fig. 2).

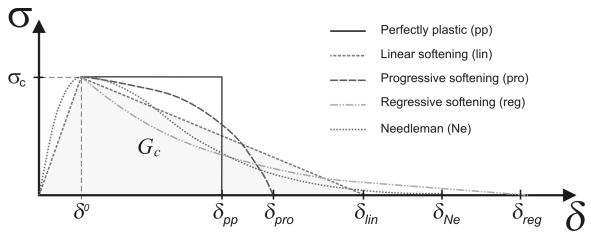

Figure 2. Strain softening constitutive models.

Bilinear Softening Model

The linear elastic-linear softening (bilinear) model is the simplest to implement, and is most commonly used [1; 5; 6]. The double cantilever beam test shown in Fig. 3 illustrates the material response. The stress σ represents a normal or tangential traction between the top and bottom faces of the element, which is a function of the relative normal or tangential displacement δ. Point 1 in the plot and the DCB shown in Fig. 3 corresponds to a material location subjected to a low tensile load that is within the elastic range. A high initial stiffness K_p (penalty) holds the top and bottom faces of the interface element together. Point 2 represents the onset of damage. In single-mode delamination, the traction at point 2 is equal to the corresponding interlaminar strength of the material, σ_c. As the relative displacement increases, the interface accumulates damage and the traction is lower than the strength (point 3). The energy dissipated damaging the surface at point 3 is the area of the triangle 0-2-3. The energy released is the most important component of the failure criterion described in the next section. If the load were to reverse, point 3 would unload to the origin, as shown in the figure.

The critical value of the energy release rate is attained at point 4. For any relative displacement larger than point 4, the interface does not carry any tensile or shear loads (point 5). In other words, at point 4 all the available interfacial fracture energy has been completely consumed. Note that when modeling delamination with a softening response, the delamination tip is not defined explicitly. While the onset of damage occurs at point 2 in Fig. 4, the delamination tip could be defined as the point where the tractions at the interface are zero, which is point 4.

The softening response illustrated in Fig. 3 is representative of the tension or the shear response but not compression. It is assumed that compression loads do not cause delamination or softening, and the effect of compression on damage of the interface was neglected in the present work.

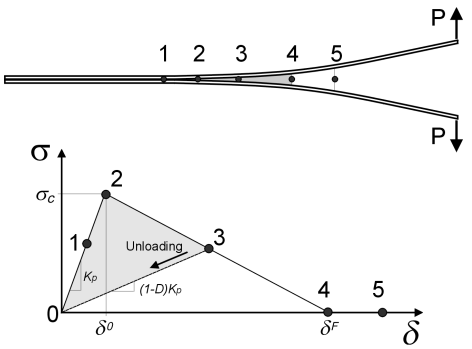

Figure 3. Bilinear constitutive model.

The problem of contact of the crack faces after failure is addressed by re-applying the normal penalty stiffness. The process of reapplying the normal stiffness when interpenetration is detected is typical of solution procedures of contact problems using penalty methods in a constrained variational formulation.

Mixed-Mode Delamination Criterion

Under pure Mode I, II or III loading, the onset of damage at the interface can be determined by comparing the stress components with their respective allowables. Under mixed-mode loading, however, damage onset may occur before any of the stress components involved reach their respective allowables. The mixed-mode criterion proposed by the authors in Ref. 2 assumes delamination initiation can be predicted using a failure criterion based on a quadratic interaction between the interlaminar stresses. In addition, it is also assumed that the delamination growth is governed by a quadratic interaction among the energy release rates corresponding to the opening (Mode I) and tangential (Modes II and III) displacements.

The element stiffness matrix is calculated based on the standard isoparametric linear Lagrangian interpolation functions for three-dimensional (8-node) elements. The element was implemented into an ABAQUS user-written subroutine (UEL)[7]. The details of the formulation can be found in Refs. 1 and 2.

PLY DAMAGE

To simulate damage growth accurately, the failure analysis must be able to predict the failure modes in each ply and apply the corresponding reduction in material stiffnesses. The failure criteria included in the present analyses are those proposed by Hashin [8] and are summarized below.

Matrix Failure in tension and compression occurs due to a combination of transverse stresses, σ_{22}, σ_{33}, and shear stresses, τ_{12}, τ_{13} and τ_{23}. The failure index can be defined in terms of these stresses and the strength parameters Y and shear allowables S_c. Failure occurs when the index exceeds unity. Assuming linear elastic response, the failure index has the form:

$$e_m^2 = \left(\frac{\sigma_{22}+\sigma_{33}}{Y_c}\right)\left(\left(\frac{Y_c}{2S_{c23}}\right)^2 - 1\right) + \left(\frac{(\sigma_{22}+\sigma_{33})^2}{4S_{c23}^2}\right) + \left(\frac{\tau_{12}}{S_{c12}}\right)^2 + \left(\frac{\tau_{13}}{S_{c13}}\right)^2 + \left(\frac{\tau_{23}}{S_{c23}}\right)^2 - \left(\frac{\sigma_{22}\sigma_{33}}{S_{c23}^2}\right) \quad \text{for} \quad (\sigma_{22}+\sigma_{33}) < 0 \tag{2}$$

and

$$e_m^2 = \left(\frac{\sigma_{22}+\sigma_{33}}{Y_t}\right)^2 + \left(\frac{\tau_{12}}{S_{c12}}\right)^2 + \left(\frac{\tau_{13}}{S_{c13}}\right)^2 + \left(\frac{\tau_{23}}{S_{c23}}\right)^2 \quad \text{for} \quad (\sigma_{22}+\sigma_{33}) \geq 0 \tag{3}$$

where Y_t is the strength perpendicular to the fiber direction in tension, Y_c is the strength perpendicular to the fiber direction in compression, and S_{c12}, S_{c13}, and S_{c23} are the in-plane shear and transverse shear strengths, respectively.

Fiber-matrix failure occurs due to a combination of axial and shear stresses. The failure criterion has the form:

$$e_s^2 = \left(\frac{\sigma_{11}}{X_c}\right)^2 + \left(\frac{\tau_{12}}{S_{c12}}\right)^2 + \left(\frac{\tau_{13}}{S_{c13}}\right)^2 \quad \text{for} \quad \sigma_{11} < 0 \tag{4}$$

and

$$e_s^2 = \left(\frac{\tau_{12}}{S_{c12}}\right)^2 + \left(\frac{\tau_{13}}{S_{c13}}\right)^2 \quad \text{for} \quad \sigma_{11} \geq 0 \tag{5}$$

where X_t is the strength along the fiber direction in tension, and X_c is the strength along the fiber direction in compression.

Fiber failure in tension or compression occurs independently of other stress components. In compression the fiber fails by buckling. The failure criterion has the form:

$$e_f = -\frac{\sigma_{11}}{X_c} \quad \text{for} \quad \sigma_{11} < 0 \tag{6}$$

and

$$e_f = \frac{\sigma_{11}}{X_t} \quad \text{for} \quad \sigma_{11} \geq 0 \tag{7}$$

To simulate the above failure modes, the elastic properties are made to be linearly dependent on three field variables, *FV1* through *FV3*. The first field variable represents matrix damage, the second the fiber-matrix shearing, and the third the fiber buckling failure. The values of the field variables are set to zero in the undamaged state. After the failure index has exceeded *1.0*, the associated user-defined field variable is set to *1.0*. The associated field variable then continues to have the value of *1.0*, even though the stresses may reduce to values lower than the failure of the material. This procedure ensures that the damaged material does not "heal". The mechanical properties in the damaged area are reduced appropriately, according to a pre-defined degradation schedule. For example, when the matrix failure criterion takes

the value of *1.0*, the transverse shear modulus E_y and Poisson ratio ν_{12} are set equal to zero. The field variables can be made to transition from *0* (undamaged to *1* (fully damaged) instantaneously.

The finite element implementation of this failure analysis was developed for the ABAQUS structural analysis program using the USDFLD user-written subroutine [7]. ABAQUS calls the USDFLD subroutine at all material integration points of elements that have material properties defined in terms of the field variables. The subroutine provides access points to a number of variables, such as stresses, strains, material orientation, current load step, and material name, all of which can be used to compute the field variables. Additional details on the procedure can be found in Ref. 9.

The procedure for the simulation of ply damage can be applied in conjunction with decohesion elements to model delamination growth. The following sections describe analyses of skin/stringer debonding in which ply damage and delamination growth are modeled simultaneously.

ANALYSES OF SKIN-STRINGER SPECIMEN

Extensive testing of the skin-stringer flange debonding problem has been performed by Cvitkovich and O'Brien [10; 11], and analyses have been conducted by Krueger and O'Brien [12]. The configuration of the specimens studied in Refs. 10 and 12 is shown in Fig. 4. The specimens are 203 mm.-long and 25.4 mm.-wide. Both skin and flange are made from IM6/3501-6 graphite/epoxy prepreg tape with a nominal ply thickness of 0.188 mm. The skin lay-up consisting of 14 plies is $[0/45/90/-45/45/-45/0]_s$ and the flange lay-up consisting of 10 plies is $[45/90/-45/0/90]_s$. Two loading configurations were considered: tension and three-point bending.

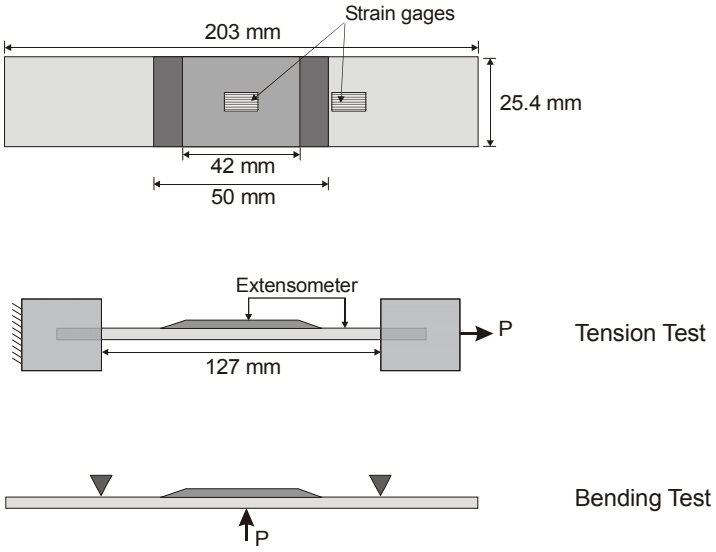

Figure 4. Skin-stringer specimen and test configurations.

Reference 12 describes the complexities of this problem, such as the presence of several interacting failure modes, a non self-similar crack growth, and crack fronts that jump between plies and do not remain at a single interface. References 10 and 12 also show that delamination seldom initiates or grows between the flange and the skin, but rather on a surface one or two plies away from the skin-flange interface. A photo micrograph taken from Ref. 10 and shown in Fig. 5 shows these features.

The moduli and strength properties of the unidirectional graphite/epoxy and the the interface reported in Refs. 9 and 12 are shown in Tables 1, 2, and 3, respectively.

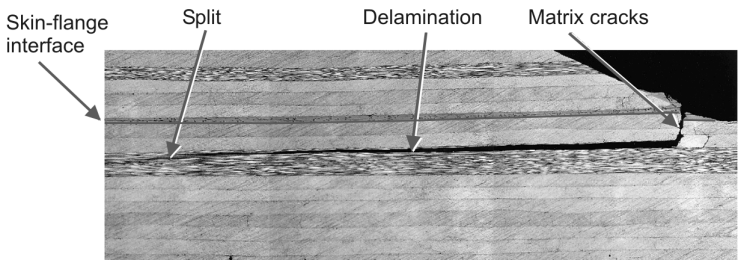

Figure 5. Detail of debond area in a failed specimen [11].

Table 1. Elastic properties of unidirectional IM6/3501-6 graphite/epoxy [12].

E_{11}	$E_{22}=E_{33}$	$\nu_{12}=\nu_{13}$	ν_{23}	$G_{12}=G_{13}$	G_{23}
144.7 GPa	9.65 GPa	0.3	0.45	5.2 GPa	3.4 GPa

Table 2. Strength properties of unidirectional IM6/3501-6 graphite/epoxy [9].

X_t	X_c	Y_t[12]	Y_c	$S_{12}=S_{13}$	S_{23}
1450 MPa	1130 MPa	61 MPa	250 MPa	142 MPa	68 MPa (est.)

Table 3. Properties of the interface[12].

G_{Ic}	G_{IIc}	Z_t	S_{LT}
0.075 N/mm	0.60 N/mm	61 MPa	68 MPa (est.)

Simplied Model of Skin-Stringer Specimen

To perform fracture mechanics calculations of skin/stringer debonding, Krueger [12] developed detailed two-dimensional models with up to four elements per ply thickness in which the discrete matrix cracks and the specific delamination paths observed in the experiments were modeled. Such level of detail may not be practical for design analyses, especially for components in which the crack paths have not been determined experimentally beforehand.

The objective of the present work is to demonstrate a methodology with predictive capabilities applicable to larger structural components. Consequently, simplifications were performed to ease the development of the model and to reduce the number of de-

grees of freedom while retaining the ability to predict accurately the debond load and the subsequent response. A relatively coarse three-dimensional model with 15,212 degrees-of-freedom was developed in which the thickness of the skin and the flange are represented by only two brick elements each. The delamination was assumed to occur at the interface between the skin and the flange, although the experiments indicate that it always develops one or two plies above or below the interface. To prevent delamination from occurring at both ends of the flange simultaneously, symmetry in the model was perturbed by modeling the taper of the flange with a refined mesh on one end and a coarser mesh on the other.

Unsymmetric layered properties were assigned to the three-dimensional elements by using the composite solid section option in ABAQUS. This option calculates the element's stiffness by performing a Simpson's integration through the thickness using material points in each of the plies within the element. Approximations were necessary in the tapered sections of the flange because planes of integration cannot be defined parallel to the plies in the tapered elements, as illustrated in Fig. 6.

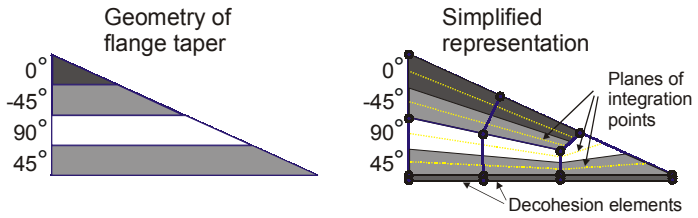

Figure 6. Detail of flange tip geometry and corresponding FE model.

Interacting Matrix Cracking and Delamination

The methodology proposed herein models the simultaneous accumulation of ply damage and delamination growth. Furthermore, the load incrementation procedure represents the interactions among the different failure modes by taking into account the load redistribution that results from any type of damage. However, a continuum damage model does not adequately represent the interaction between transverse matrix cracks and delamination. For instance, when the matrix crack in Fig. 5 reaches the 45º ply beneath it, the crack turns and initiates a delamination. The effect of matrix cracks on the model can be the opposite: a flange element with matrix cracks softens and it no longer carries the loads necessary to cause a delamination. To address the issue, it was assumed that the decohesion elements outboard of a flange element with transverse matrix cracks should be removed. Unfortunately, the current version of ABAQUS Standard (V6.2) does not support automatic element erosion. Therefore, it was necessary to manually disable the corresponding elements and to restart the analysis from the load increment in which the matrix cracks were detected.

Simulation of Tension Test

The boundary conditions for the tension test are shown in Fig. 4. The mechanism for debonding under axial load is primarily by shear lag. Deformed plots of the finite element model immediately before and after flange separation are shown in Fig. 7 with a displacement magnified 8 times. The figure shows that the refined end of the flange debonds and the coarse end does not. A detailed analysis of the results indicated that the coarse end of the flange also softens, but that the separation of the flange at the refined end relieves the stresses at the other end. Interestingly, static tests exhibit debond of only one end, while fatigue tests induce debonding at both ends.

Figure 7 also shows that the debond growth is not symmetric: the debond initiates on the left corner of the flange shown on the top of Fig. 7 due to the unsymmetry introduced by the terminated plies at the flange tapered ends. Cvitkovich [10] also commented on the difference in the modes of failure of the two corners.

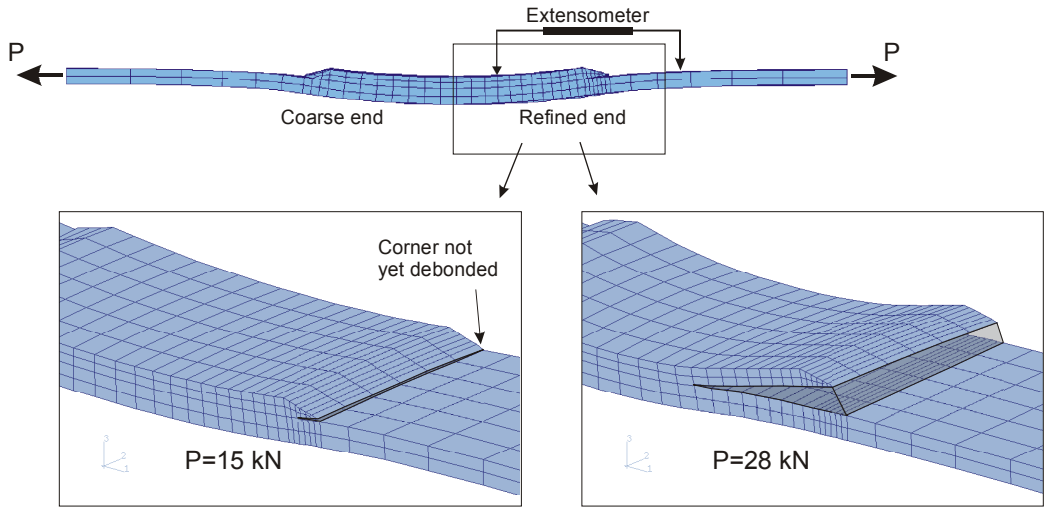

Figure 7. Deformed plots of skin/stringer model at applied loads of 15 and 28 kN (8X magnified).

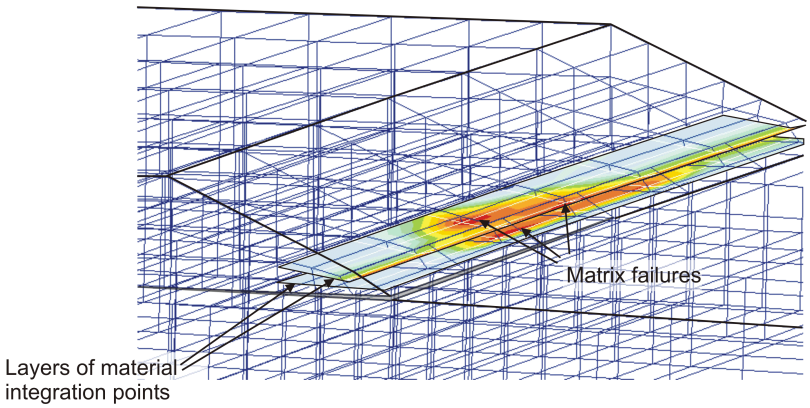

Figure 8. Matrix failures at the tip of the flange.

The damage initiation mode is by matrix failure at the 45-degree ply of the first row of elements, as shown in Fig. 8. It can be observed that the damage is non-symmetric due to the 45-degree ply which is longer at the taper, as shown in Fig. 6.

The axial strains from the two gages shown in Fig. 4 are are compared to the present analytical results in Fig. 9. The strains and the failure load predicted by the model correlate well with the test results. However, the test results after the debond load are misleading because the load was immediately reversed after failure by the test operator, even if the specimen could carry a higher load. The predicted load at failure is 23.9 kN, which is only 1.3% higher than the highest debond load measured. It is interesting to note that the debond load predicted by ignoring all damage modes except delamination is 24.1 kN, which confirms that the failure of the skin/stringer specimens is dominated by delamination.

The extensometer measurements for tests C4, C6, C8 and C10 conducted by Cvitkovich [10] and the predicted values are compared in Fig. 10. The initiation of delamination is marked by the sharp breaks in the extensometer readings. After failure, the extensometer measurements are unreliable, as can be observed by comparing the different tests. The predicted response correlates well with the experimental results. The predicted debond load is only 4% higher than the range for all four tests.

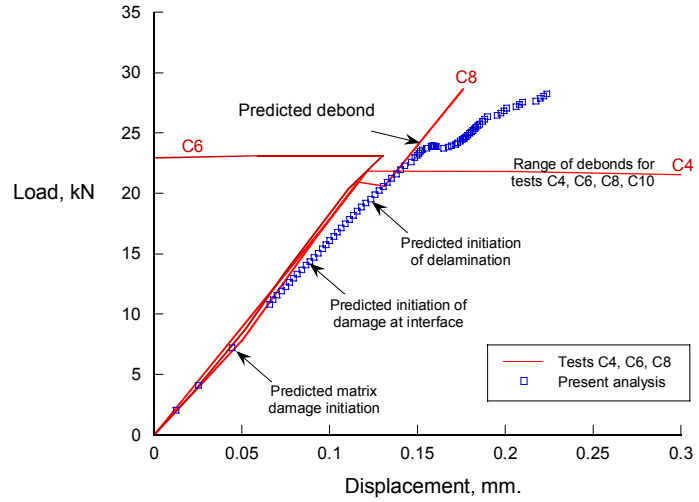

Figure 9. Strains at two gage locations for test and analysis (tension test).

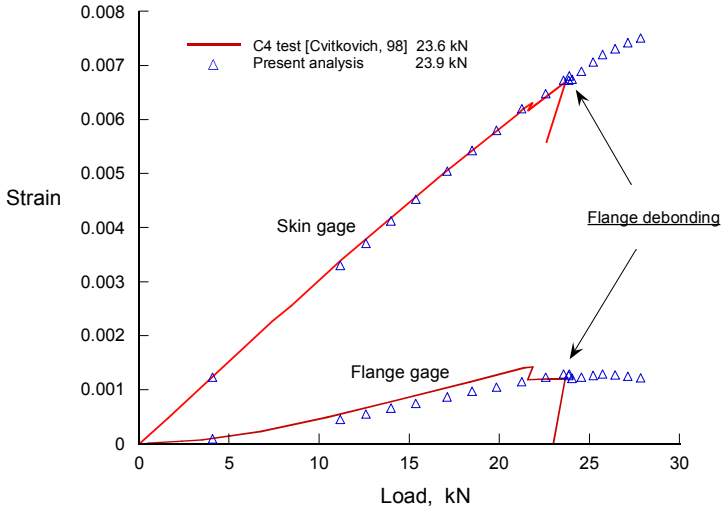

Figure 10. Predicted and experimental extensometer measurements for tension test.

Simulation of Bending Test

The boundary conditions for the three-point-bending test are shown in Fig. 4. The mechanism for the initiation of debonding under axial load is a combination of peel and interlaminar shear. The initial damage event consists of matrix cracks in the 90-degree ply of the flange taper at a load of 405 N (damage location #1 in Fig. 11). It is assumed that the row of elements at the flange tip do not carry loads, so that the first row of decohesion elements (row A) is manually eroded, as explained previously. The

second damage event occurs at 460 N, and it consists of matrix cracks in the 45-degree ply (damage location #2 in Fig. 11). At this load, the next two rows of decohesion elements are eroded (rows B and C).

Undeformed and deformed plots of the finite element model are shown in Fig. 12, where the displacements have been scaled by 200% for clarity. At the final mid-span displacement of 6.5 mm., nearly half of the flange has debonded.

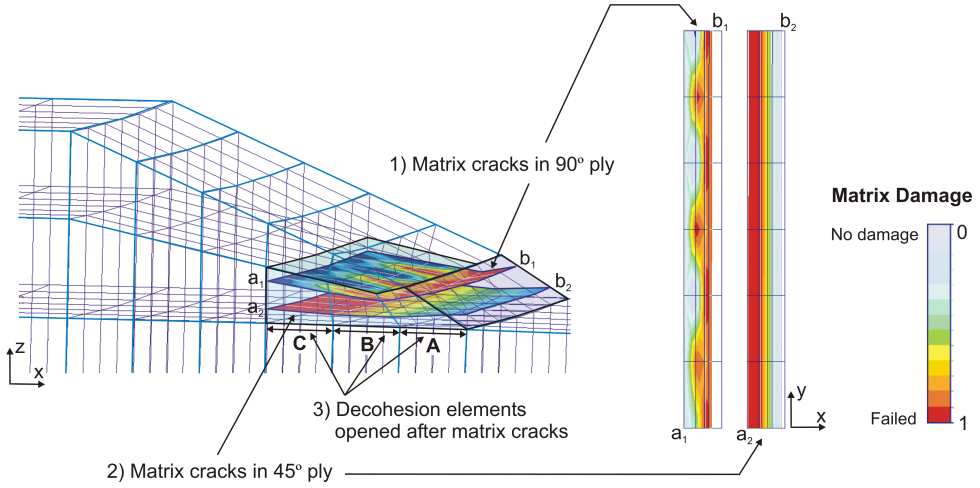

Figure 11. Sequence of initial damage events at flange tip (load=460 N.)

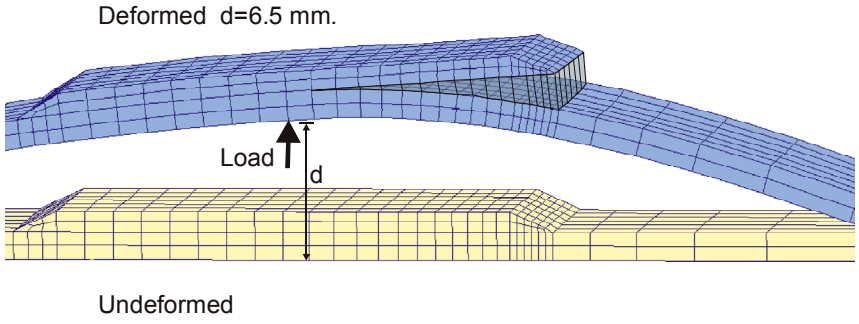

Figure 12. Undeformed and deformed plots of skin/stringer model in three-point bending.

The load-deflection curves for the tests and the simulation are shown in Fig. 13. It can be observed that the analysis overpredicts the debond load by 20%. The analysis predicts an initial unstable delamination (load reduction) of approximately ¼ of the span of the flange, followed by additional marginally stable growth at a nearly constant load of 600 N until half of the flange has debonded. In contrast, the test specimens exhibited an unstable growth of approximately half of the span of the flange. The difference between the experimental observation and the prediction can be

attributed to the dynamic effects of crack propagation, which are not considered in the simulation.

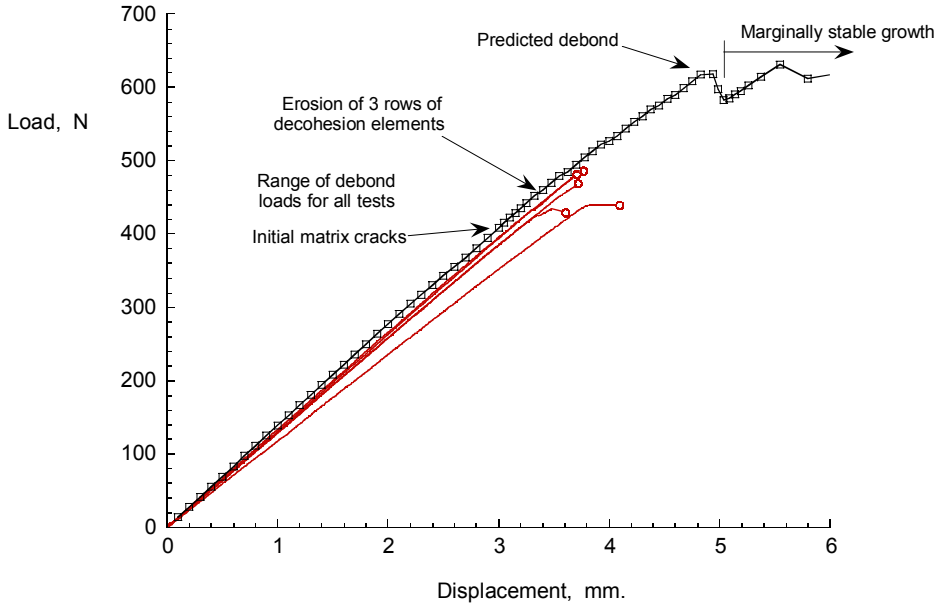

Figure 13. Predicted and experimental load-deflection curves for bending test.

CONCLUDING REMARKS

A methodology that can simulate the accumulation of ply damage and delamination growth was developed. Decohesion elements were used to model the initiation and growth of delamination, while a more conventional property degradation procedure was used to simulate ply damage modes such as matrix damage and fiber failures. The methodology was applied to the prediction of the debond loads of skin and streinger, a problem clearly dominated by delamination but where other damage mechanisms are also active. Two specimen configurations were analyzed: a tension test and a three-point-bending test. The predicted debond loads for both configurations agree well with the test results. However, it was found that a continuum damage model for the transverse matrix cracks does not provide the adequate conditions to initiate the delaminations observed in the tests. The difficulty was successfully resolved by manually initiating a delamination under the elements exhibiting transverse matrix cracks.

REFERENCES

1. de Moura, M. F. S. F., J. P. M. Gonçalves, A. T. Marques, and P. M. S. T. de Castro. 2000. "Prediction of compressive strength of carbon-epoxy laminates containing delamination by using a mixed-mode damage model," *Composite Structures*, 50: 151-157.
2. Dávila, C. G., P. P. Camanho, and M. F. S. F. de Moura. 2001. "Mixed-Mode Decohesion Elements for Analyses of Progressive Delamination," presented at the 42nd AIAA/ASME/ASCE/AHS/ASC Structures, Structural Dynamics and Materials Conference, Seattle, Washington, April 16-19, 2001.
3. Needleman, A. 1987. "A Continuum Model for Void Nucleation by Inclusion Debonding," *Journal of Applied Mechanics*, 54: 525-531.
4. Rice, J. R. 1968. "A Path Independent Integral and the Approximate Analysis of Strain Concentration by Notches and Cracks," *Journal of Applied Mechanics*: 379-386.
5. Gonçalves, J. P. M., M. F. S. F. de Moura, P. M. S. T. de Castro, and A. T. Marques. 2000. "Interface Element Including Point-to-Surface Constraints for Three-Dimensional Problems With Damage Propagation," *Engineering Computations*, 17(1): 28-47.
6. Chen, J., M. A. Crisfield, A. J. Kinloch, E. P. Busso, F. L. Matthews, and Y. Qiu. 1999. "Predicting Progressive Delamination of Composite Material Specimens Via Interface Elements," *Mechanics of Composite Materials and Structures*, 6: 301-317.
7. 2000. *ABAQUS User's Manual*, Hibbitt, Karlsson & Sorensen, Pawtucket, RI.
8. Hashin, Z. 1980. "Failure Criteria for Unidirectional Fiber Composites," *Journal of Applied Mechanics*, 47: 329-334.
9. Dávila, C. G., D. R. Ambur, and D. M. McGowan. 2000. "Analytical Prediction of Damage Growth in Notched Composite Panels Loaded in Compression," *Journal of Aircraft*, 37(5): 898-905.
10. Cvitkovich, M. K., R. Krueger, T. K. O'Brien, and P. J. Minguet. 1998. "Debonding in Composite Skin/Stringer Configurations Under Multi-Axial Loading," presented at the American Society for Composites - 13th Technical Conference on Composite Materials, Baltimore, MD, September 21-23, 1998, 1014-1048.
11. Cvitkovich, M. K., T. K. O'Brien, and P. J. Minguet. 1997. "Fatigue Debonding Characterization in Composite Skin/Stringer Configurations," Hampton, VA.
12. Krueger, R., M. K. Cvitkovich, T. K. O'Brien, and P. J. Minguet. 2000. "Testing and Analysis of Composite Skin/Stringer Debonding Under Multi-Axial Loading," *Composite Materials*, 34(15): 1263-1300.

ACKNOWLEDGEMENTS

The authors gratefully acknowledge Drs. Ronald Krueger and Isabelle Paris for providing insight and experimental results on the specimens analyzed in this paper.